crystals

MDPI

Article

Influence of Temperature on the Moisture Transport in Concrete

Qingzhang Zhang [1,2], Zihan Kang [1], Yifeng Ling [3,*], Hui Chen [4] and Kangzong Li [1]

1 College of Civil Engineering, Henan University of Technology, Zhengzhou 450001, China; zqz313@haut.edu.cn (Q.Z.); kzhsgdsb@163.com (Z.K.); lkz857@163.com (K.L.)
2 Key Laboratory of Performance Evolution and Control for Engineering Structures of Ministry of Education, Tongji University, Shanghai 200092, China
3 School of Qilu Transportation, Shandong University, Jinan 250002, China
4 Department of Architecture and Civil Engineering, Oujiang College, Wenzhou University, Wenzhou 325035, China; chenhui0306@wzu.edu.cn
* Correspondence: jemeryling@gmail.com

Abstract: Moisture with harmful ions penetrates into the interior of concrete, which causes deterioration of the concrete structure. In this study, a moisture saturation equilibrium relationship of concrete was tested under different temperatures and relative humidity conditions to develop moisture absorption and desorption curves. Based on experimental data and numerical simulation, a model of moisture transport in concrete was established. The results from the model indicate that the moisture absorption rate was lower at higher temperatures and largely dependent on the saturation gradient, while the desorption was increased at higher temperatures and mostly affected by the saturation gradient. The proposed model was highly in agreement with the experimental data.

Keywords: concrete; humidity; moisture absorption; moisture desorption; numerical simulation

Citation: Zhang, Q.; Kang, Z.; Ling, Y.; Chen, H.; Li, K. Influence of Temperature on the Moisture Transport in Concrete. *Crystals* **2021**, *11*, 8. https://dx.doi.org/10.3390/cryst11010008

Received: 9 December 2020
Accepted: 21 December 2020
Published: 23 December 2020

1. Introduction

The inevitable ingress of moisture with harmful ions into concrete could reduce the pH value of pore solution. Temperature is a key factor in the rate of moisture transport in concrete because it can change pore pressures to cause concrete spalling at a critical degree [1–3]. The rate of moisture transport in concrete directly affects the time and degree of concrete deterioration. Therefore, understanding the moisture transport process in concrete is essential to design durable concrete structures [4–6]. The main factors determining the rate of moisture transport in concrete include temperature, relative humidity (RH), microstructure and porosity of concrete.

The isothermal absorption and desorption of moisture vapor in a cement-based material reflect the ability of its pore structure to absorb and desorb moisture [7]. Therefore, the moisture absorption and desorption processes are typically characterized using isothermal absorption–desorption curves [8]. Concrete under an environment with different RH levels will finally attain an equilibrium state at a constant temperature when the pore structure reaches a particular moisture saturation level [9]. The Young-Laplace equation describes the relationship between the capillary pressure and aperture, while the Kelvin equation expresses gas–liquid equilibrium relationship between the curvature of liquid surface and vapor pressure. These two equations can be used to transform the isothermal absorption–desorption curve so as to represent the relationship between the capillary pressure and saturation [10,11]. Trabelsi et al. developed an isothermal absorption–desorption curve to describe the moisture desorption using statistical and finite element methods [12]. Neithalath et al. [13] calculated the intrinsic permeability of concrete based on the porosity, specific surface area and tortuosity. Baroghel-Bouny et al. [14] obtained isothermal desorption curves for concrete and determined a theoretical relationship between the relative permeability coefficient and saturation based on findings in the literature [15]. The diffusion

coefficient of moisture in concrete was determined, and then the moisture transfer curves under the drying process were obtained.

Zhou and Li [16] studied the concrete permeability using a three-phase composite random aggregate concrete simulation model based on the finite element method. Wang and Ueda [17] discretely divided concrete at the mesoscale to characterize moisture transport and investigated the influence of the interfacial transition zone on the capillary absorption of the concrete. Li et al. [18] established a three-dimensional mesoscale model to evaluate concrete permeability.

In previous numerical studies on moisture transport, the parameters that determine the influences of temperature and RH in the driving force of capillary pressure, have not been derived. In this paper, isothermal adsorption and desorption experiments were carried out at three temperatures (20 °C, 35 °C, 50 °C) to obtain the adsorption–desorption curves. The influences of different temperatures and RHs on the moisture transport process of concrete were analyzed. Further, a model in function of RH and saturations of adsorption and desorption process was regressed based on experimental data. Using the Kelvin equation, the relationship between capillary pressure and saturation was evaluated. A moisture transport model in respect of capillary pressure and saturation of concrete was established and verified with the experiment results. In addition, the moisture transport behavior of concrete at different temperatures and RHs was simulated.

2. Materials and Methods

2.1. Test Materials

Concrete was made of cement, mineral powder, fine aggregate, and coarse aggregate. The binder material comprised P.O42.5 ordinary Portland cement and mineral powder with densities of 3060 and 2890 kg/m^3 respectively, in equal mass fraction. The chemical composition of cement is shown in Table 1. The fine aggregate was well-graded medium sand with a measured apparent density of 2623 kg/m^3 (Table 2). The coarse aggregate had a 5–20 mm continuous particle gradation, a maximum particle size of 20 mm (Table 3), and a measured apparent density of 2710 kg/m^3. The fresh concrete was cast into 120 molds in dimensions of 100 mm × 100 mm × 100 mm. After curing at 20 ± 2 °C and 95% RH for 28 days, each specimen was cut horizontally into three pieces in a dimension of 100 mm × 100 mm × 30 mm. To avoid separation from vibration, only the middle piece was selected for testing. In total, 60 absorption and 60 desorption specimens were prepared. Table 4 provides the mix proportion of concrete in accordance with previous studies [19–21].

Table 1. Chemical compositions of cement in mass.

Composition	SiO_2	Fe_2O_3	Al_2O_3	CaO	MgO	Na_2O	SO_3
%	22.4	3.7	4.7	60.3	2.7	0.13	2.1

Table 2. Particle size distribution of fine aggregate.

Size of Screen Mesh (mm)	4.75	2.36	1.18	0.60	0.30	0.15
Passing percent (%)	99.5	87.7	72.0	45.9	19.6	2.1

Table 3. Particle size distribution of coarse aggregate.

Size of Screen Mesh (mm)	26.5	16	9.5	4.75	2.36
Passing percent (%)	100.0	76.0	14.4	0.3	0.0

Table 4. Concrete mix ratio for the absorption and desorption specimens.

Water kg/m^3	Binder Material kg/m^3	Fine Aggregate (Sand) kg/m^3	Coarse Aggregate kg/m^3
261.0	562.0	514.0	960.0

2.2. Test Method

The tests were performed as per ISO12571-2013 [22]. The specimens for the absorption test were first oven-dried at 100 °C for 24 h and then placed in a dryer to cool down to 20 °C (room temperature) and weighed. Subsequently, all specimens were oven-dried for another 12 h, cooled down to 20 °C in the dryer and weighed. These steps were repeated until the change in mass was less than 0.5% to obtain a dry state. For the desorption test, all dry specimens were placed in water for seven days to be saturated, surface-dried with a towel and weighed. Then, the specimens were returned to the water for 24 h and weighed. This was repeated until the change in the specimen mass was less than 0.5% to obtain a saturated state.

Afterward, the specimens were moved to glass containers in a constant-temperature/humidity chamber with a temperature accuracy of ±1 °C and 50 ± 2% RH as shown in Figure 1. During the test, saturated salt solutions of LiCl, $MgCl_2$, KBr and KNO_3 were added at the bottom of glass containers to secure 10%, 35%, 80% and 95% RH respectively. It should be noted that for the specimens at 50% RH, there was no saturated salt solution. The testing temperatures were 20 °C, 35 °C and 50 °C.

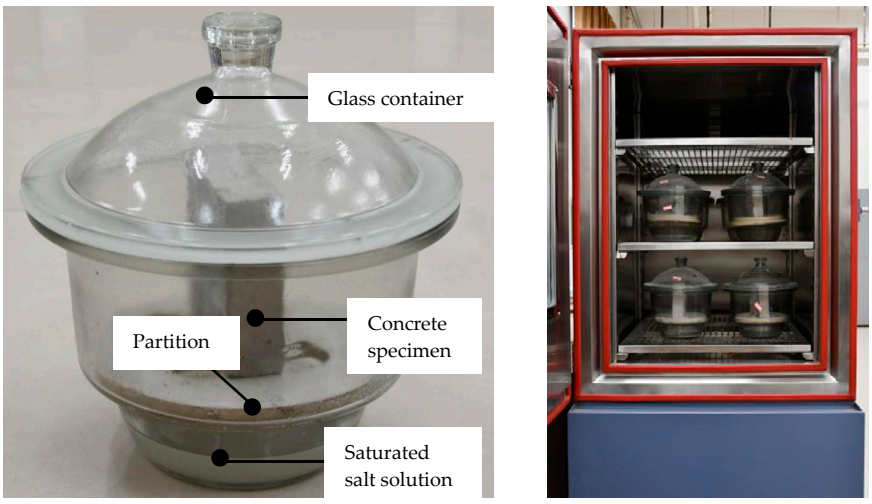

Figure 1. Isothermal adsorption devices (**a**) glass container, (**b**) constant-temperature/humidity chamber.

Each specimen was weighed at designated time interval until the change in mass was less than 0.1%. It should be noted that since the mass change was decreasing over time, the time interval of weight measurement in the early stage was shorter than in the later stage. In total, there were 12 weight measurements for the absorption test and 13 weight measurements for the desorption test.

The specimens were designated as X-% and P-% for the absorption and desorption tests, respectively. The percentage represented the RH conditions. For example, specimens X-10% is the absorption specimens for 10% RH.

2.3. Determination of Saturation

The moisture content of a specimen can be defined as follows [8]:

$$S = \frac{V_S}{V_\phi} \tag{1}$$

where S is the moisture saturation, V_S is the volume occupied by water in the pores of the specimen, and V_ϕ is the volume of pores in the specimen.

In order to determine adsorption and desorption isotherms, the moisture saturation S can be expressed based on the water content [23]:

$$S = \frac{m_{\mathrm{w}} - m_{\mathrm{d}}}{m_{\mathrm{ws}} - m_{\mathrm{d}}} \tag{2}$$

where m_w is the mass of specimen underwater (kg), m_d is the mass of the specimen in a dry state (kg) and m_{ws} is the mass of the specimen under saturation state (kg).

3. Results and Discussion

3.1. Absorption–Desorption Curves

Absorption mainly refers to physical absorption, which is the phenomenon that moisture enters concrete through capillary pressure, while desorption is the phenomenon that moisture in concrete is transferred from liquid to gas and released from concrete.

Absorption–desorption curves representing the changes in the moisture contents of the specimens over time at 20, 35, and 50 °C are shown in Figure 2.

Figure 2a shows that, at the same temperature, the absorption curves tended to be consistent between the different RH conditions, as the specimen saturation increased significantly during the initial stage of the absorption process. As absorption progressed, the saturation between the interior and exterior of concrete decreased due to decreased moisture absorption capacity and eventually stabilized. The moisture absorption behaviors of the specimens were similar at different temperatures. For a given temperature, a higher RH resulted in faster moisture absorption. When the RH was lower than 50%, the moisture-absorption process of the specimen was gradual, which reveals that temperature and RH had little effect on the time required to reach the equilibrium. The absorption rate and capacity increased sharply when the RH was greater than 50%. At 80% RH, the moisture absorption capacity and equilibrium time both increased as temperature decreased. Under low-RH conditions (i.e., less than 50% RH), the concrete exhibited less moisture absorption capacity with saturation less than 0.1, and temperature's effect on the moisture absorption rate was marginal. When RH was greater than 50%, temperature's effect on the moisture absorption became significant.

During the desorption test, a lower RH came with a greater saturation between the interior and exterior of concrete, and a longer time to reach equilibrium, as shown in Figure 2b. When the RH was lower than 80%, the increment of temperature increased desorption capacity and the time to reach equilibrium. When RH was higher than 80%, the effect of temperature on the moisture transport rate decreased. Regardless of temperature, the saturation at equilibrium was approximately 0.9.

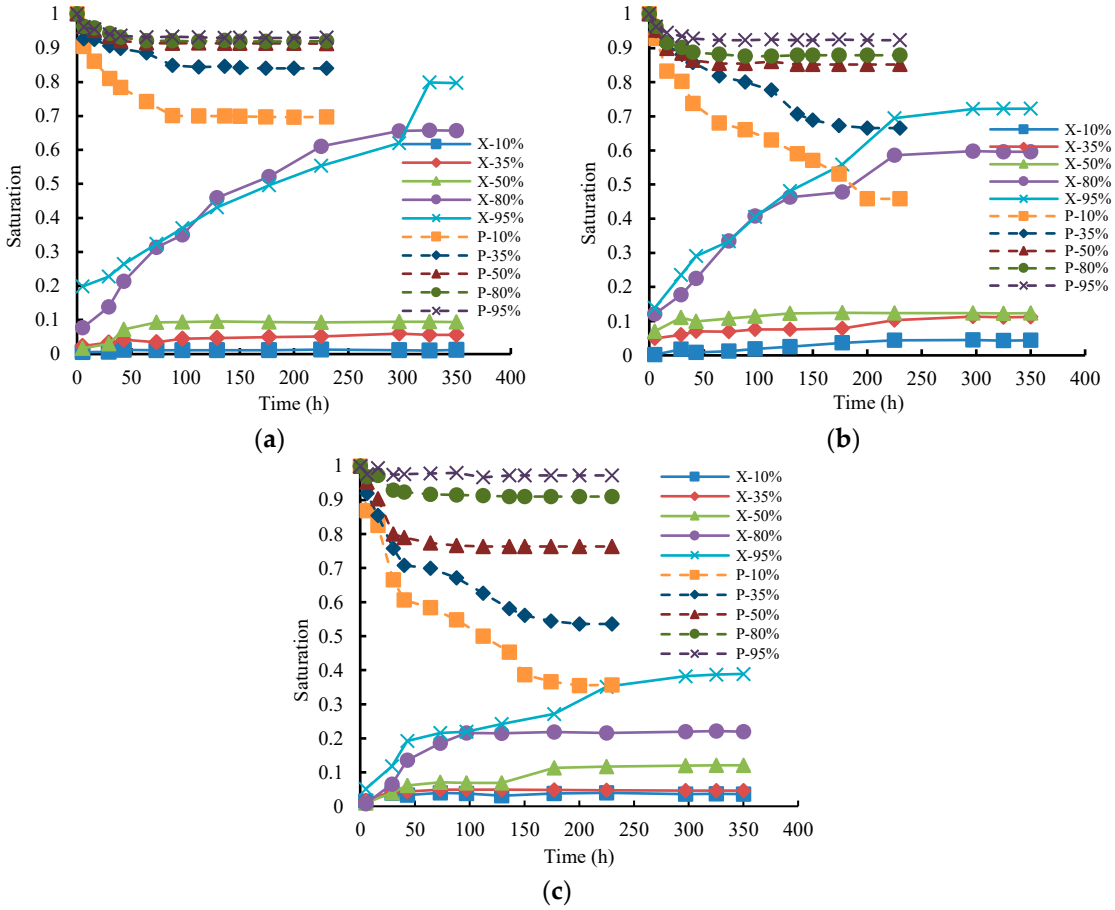

Figure 2. Absorption and desorption over time: (**a**) 20 °C, (**b**) 35 °C, (**c**) 50 °C.

3.2. RH–Saturation Equilibrium

The RH–saturation curves during absorption and desorption for different RH conditions are shown in Figure 3. The curves were substantially similar for different temperatures. As RH increased, the saturation gradually increased. When RH was below 50%, the absorption process was gradual. The absorption capacity significantly increased when RH was greater than 50%. Irrespective of temperature, 50% RH was an inflection point in the moisture absorption process. Based on the Kelvin equation, the maximum pore size that could be saturated was approximately 4 nm at 50% RH, and the boundary between the gel pores and capillary pores was generally 10 nm (i.e., gel pores < 10 nm < capillary pores). Therefore, when RH was below 50%, only part of the gel pores was saturated, while for RH above 50%, the capillary pores saturated gradually, thereby rapidly increasing the saturation [24]. Further, the saturation decreased with decreasing RH. As temperature decreased, the saturation considerably decreased. At 80% RH, the equilibrium saturation decreased substantially, which indicates that an RH greater than 80% could greatly affect the equilibrium of the moisture desorption process in concrete.

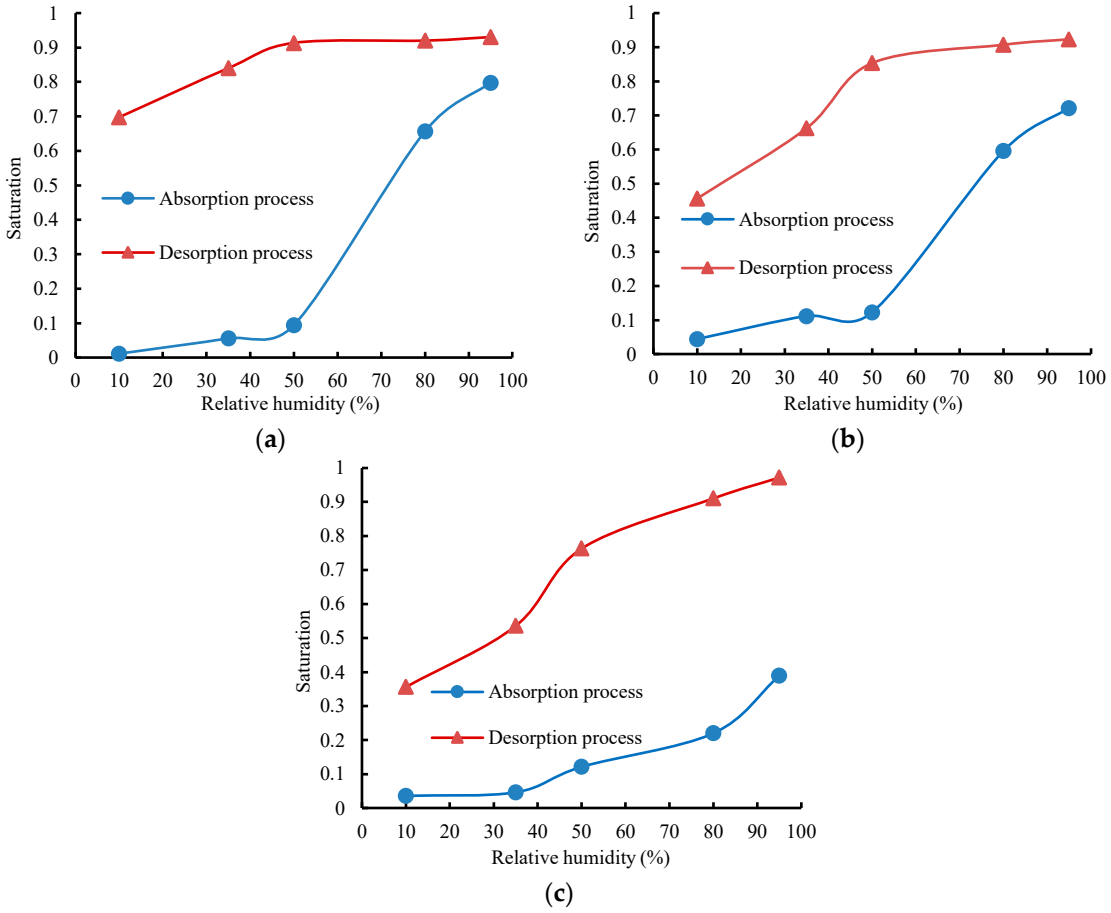

Figure 3. Absorption and desorption equilibrium curves: (**a**) 20 °C, (**b**) 35 °C, (**c**) 50 °C.

In Figure 3, since the desorption curve is above the absorption curve, it indicates a higher saturation for a given RH. The desorption process displays a significantly hysteretic nature compared to the absorption process, which implies that the gas–liquid equilibrium in pores is nonhomogeneous. The hysteresis represents the "ink bottle effect," which refers to the effect that a small pore (bottleneck) exerts stress upon the water in a connected large pore (bottle) [25]. Larger concrete capillary pores require a higher RH to reach equilibrium saturation than small pores. For initially saturated pores, the liquid water in large pores transports through the liquid water in small pores without forming a gas–liquid interface. Therefore, the water in large pores can be discharged only when the ambient RH is below the saturated RH of small pores. For a given RH, the saturation equilibrium of the moisture absorption process is lower than that of the moisture desorption process [26].

For a given RH, the capillary condensation phenomenon is more likely to occur during the absorption process, and a higher saturation can be attained at a lower temperature. During desorption, at a higher temperature, the saturation is lower because the pore water evaporates more easily [27]. According to a study by Zeng [8], the relationship between the capillary pressure and RH is:

$$p_c = \frac{\rho_l RT}{M} \ln h \tag{3}$$

where M is the molar mass of water (kg/mol), R is the gas constant (given as 8.314 J/mol/K), p_c is the capillary pressure (Pa), h is the RH, T is the absolute temperature (K) and ρ_l is the density of liquid water (kg/m^3).

Using Equation (3), the isothermal equilibrium curve of RH and concrete saturation can be converted into a moisture characteristic curve, as shown in Figure 4. When the concrete was at the same saturation through absorption and desorption, the capillary pressure of the desorbed concrete was greater than that of the absorbed concrete, reflecting

the hysteretic nature of the desorption process. When the temperature was lower during both the absorption and desorption processes, the capillary pressure was greater, as well as the equilibrium saturation corresponding to the same capillary pressure.

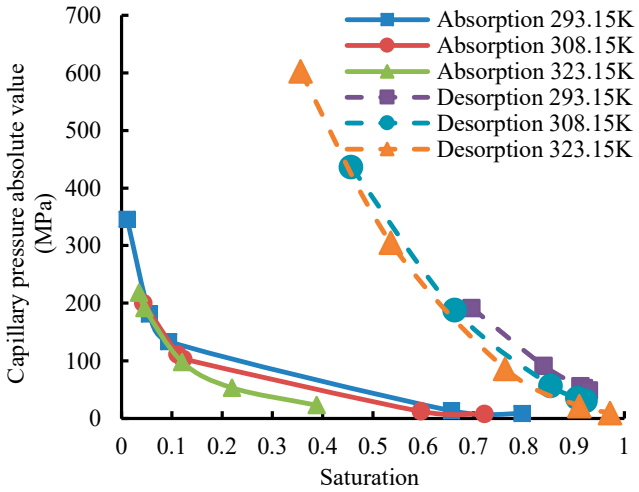

Figure 4. Equilibrium relationship between the capillary pressure and saturation.

3.3. RH and Saturation Equilibrium Model

In [28], a model representing the absorption of water by the hygroscopic material and RH is shown as follows:

$$W = [\frac{-\ln(1-h)}{A(T+B)}]^{\frac{1}{C}} \tag{4}$$

where W is the equilibrium moisture content and A, B and C are coefficients.

By replacing the equilibrium moisture content with the saturation, Equation (4) can be applied to find the inverse function. The RH and saturation relationship is:

$$h = 1 - \exp(-A(T+B)S^C) \tag{5}$$

where S is the saturation.

The model of the relationship between RH and equilibrium saturation can be obtained by substituting the data from the experimental results as seen in Figure 3 into Equation (5). Nonlinear regression was used to yield Equations (6) and (7) for the absorption and desorption processes, respectively.

$$h_{as} = 1 - \exp(-0.03(T-180.7)S^{0.837}) \qquad R^2 = 0.91 \tag{6}$$

$$h_{ds} = 1 - \exp(-0.05(T-258.76)S^{5.04}) \qquad R^2 = 0.91 \tag{7}$$

4. Moisture Transport Model

4.1. Moisture Movement in Unsaturated Concrete

The transport of liquid water in unsaturated concrete can be expressed by Darcy's law. For saturated concrete, the permeability coefficient is constant and a function of saturation for unsaturated concrete.

According to the Darcy–Buckingham equation, the relationship between transport rate of liquid water and capillary pressure is expressed as [11]:

$$v_l = -\frac{k_l}{\mu}\mathrm{grad}(p_c) \tag{8}$$

where v_1 is the rate (m/s); k_1 is the effective permeability for moisture transport (m^2), which is related to the moisture content in concrete and micro-geometric parameters of the pore occupied by moisture; μ is the dynamic viscosity coefficient of water (Pa·s).

If the conversion of liquid water to water vapor in the pores of concrete is neglected, the moisture transport in the concrete conforms to the law of mass conservation. The moisture transport equation in concrete can be written as below [29,30]:

$$\frac{\partial \theta}{\partial t} = \mathrm{div}\left[\frac{k_1}{\mu}\mathrm{grad}(p_c)\right] \tag{9}$$

Converting the left side of Equation (9) to pore moisture content and the right side into the pore moisture saturation gradient, it becomes:

$$\frac{\partial \theta}{\partial t} = \mathrm{div}\left[\frac{k_1}{\mu}\frac{\partial p_c}{\partial S}\mathrm{grad}(S)\right] \tag{10}$$

where θ is the moisture content of the concrete.

The effective permeability to moisture transport (k_1) can be expressed as

$$k_1 = k k_{rl} \tag{11}$$

Therefore, Equation (10) can be rewritten as follows:

$$\frac{\partial \theta}{\partial t} = \mathrm{div}\left[\frac{k k_{rl}}{\mu}\frac{\partial p_c}{\partial S}\mathrm{grad}(S)\right] \tag{12}$$

where k is the intrinsic permeability of concrete (m^2), and k_{rl} is the relative permeability, which is a parameter associated with the saturation.

Equation (12) can be expressed as:

$$\frac{\partial \theta}{\partial t} = \mathrm{div}[D(S)\mathrm{grad}(S)] \tag{13}$$

$$D(S) = \frac{k}{\mu}k_{rl}\frac{\partial p_c}{\partial S} \tag{14}$$

where $D(S)$ is the transport coefficient of liquid water (m^2/s).

The relationship between the dynamic viscosity coefficient of water (μ), and temperature can be expressed as follows: [31]

$$\mu = \frac{0.001775}{[1 + 0.0837(T - 273.15) + 0.000221(T - 273.15)^2]} \tag{15}$$

The intrinsic permeability (k) of concrete can be determined based on the porosity, specific surface area and tortuosity of concrete using the Kozeny–Carman model [13]:

$$k = \frac{\phi^3}{F_s \tau_c^2 \Omega^2 (1 - \phi)^2} \tag{16}$$

where F_s is the factor representing the influence of pore shape (2 for a circular and tubular pore), τ_c is the tortuosity and Ω is the specific surface.

4.2. Relationship between the Moisture Transport Parameters

By substituting Equations (6) and (7), which represent the equilibrium relationship between RH and saturation, into Equation (3), the relationship between the capillary

pressure and saturation during the moisture absorption and desorption processes can be expressed as Equations (17) and (18), respectively.

$$p_{as} = \frac{\rho_l RT}{M} \ln(1 - \exp(-0.03(T - 180.7)S^{0.837})) \quad (17)$$

$$p_{ds} = \frac{\rho_l RT}{M} \ln(1 - \exp(-0.05(T - 258.76)S^{5.04})) \quad (18)$$

The relationship between the relative permeability ($k_{rl}(S)$), and relative saturation can be established based on previous studies [14,15,32]:

$$p_c = A_a(S^{-1/m} - 1)^{1-m} \quad (19)$$

$$k_{rl}(S) = \sqrt{S}[1 - (1 - S^{1/m})^m]^2 \quad (20)$$

where m and A_a are undetermined coefficients.

The value of m can be determined through regression of the capillary pressure versus saturation curve. The absolute value of capillary pressure m for absorption and desorption processes at different temperatures can be derived based on Equation (19) through nonlinear fitting.

Using the data in Table 5 to fit the relationship between m and T for the absorption and desorption processes gives Equations (21) and (22), respectively.

$$m_{as} = 1/(2.89\ln(T) - 14.89) \quad (21)$$

$$m_{ds} = 1/(21.06 - 3.16\ln(T)) \quad (22)$$

Table 5. m values corresponding to the absorption and desorption process.

	Moisture Absorption			**Moisture Desorption**		
T(K)	293.15	308.15	323.15	293.15	308.15	323.15
m	0.672	0.579	0.573	0.328	0.324	0.362
R^2	0.985	0.988	0.991	0.999	0.997	0.992

Equations (21) and (22) are then substituted into Equation (20) to express the relationship between the relative permeability and saturation during the moisture absorption process.

$$k_{rl-as}(S) = \sqrt{S}[1 - (1 - S^{2.89\ln(T)-14.89})^{1/[2.89\ln(T)-14.89]}]^2 \quad (23)$$

Thus, the relationship between the relative permeability and saturation during the moisture desorption process is:

$$k_{rl-ds}(S) = \sqrt{S}[1 - (1 - S^{21.06-3.16\ln(T)})^{1/[21.06-3.16\ln(T)]}]^2 \quad (24)$$

4.3. Moisture Transport Model

The relationships between capillary pressure and saturation during the process of moisture absorption and desorption are shown in Equations (17) and (18). These equations are then substituted into Equation (13) to develop the moisture transport model for absorption and desorption processes.

$$\frac{\partial \phi S}{\partial t} = \mathrm{div}[D(S)\mathrm{grad}(S)] \quad (25)$$

where ϕ is the porosity of concrete.

Transport coefficient $D(S)$ of Equation (25) in absorption and desorption processes are then represented as Equations (26) and (27), respectively.

$$D_{\mathrm{as}}(S) = \frac{0.02511 k k_{\mathrm{rl-as}} \rho_{\mathrm{l}} RT(T-180.7) S^{-0.163} \exp(-0.03(T-180.7) S^{0.837})}{\mu M(1-\exp(-0.03(T-180.7) S^{0.837}))} \tag{26}$$

$$D_{\mathrm{ds}}(S) = \frac{0.252 k k_{\mathrm{rl-ds}} \rho_{\mathrm{l}} RT(T-258.76) S^{4.04} \exp(-0.05(T-258.76) S^{5.04})}{\mu M(1-\exp(-0.05(T-258.76) S^{5.04}))} \tag{27}$$

4.4. Heat Balance Equation

The heat balance equation correlated to the saturation can be established based on Fourier's law [11,33]:

$$c\rho \frac{\partial T}{\partial t} + \nabla \cdot [-\lambda_S \nabla T] = Q \tag{28}$$

where c is the specific heat of material (J/kg·K), λ_S is the thermal conductivity at different saturations (W/m·K), ρ is the material density (kg/m^3) and Q is the heat flux (J/m^2·s). The negative sign indicates that the direction of heat flow is opposite to the direction of the temperature gradient.

The transient plane source (TPS) technique was used to determine the thermal conductivity for the concrete in the same mix proportion as in the present study and at the same saturation values of 0, 0.3, 0.5, 0.7, 0.9 and 1.0 as in the moisture absorption and desorption tests described in Section 2.1. The relationship between the thermal conductivity and saturation is:

$$\lambda_S = (1 + 0.3432 S^2) \lambda_{\mathrm{a}} \tag{29}$$

where λ_{a} is the thermal conductivity under dry state (W/m·K).

5. Numerical Simulation

5.1. Model Parameters and Mesh Generation

The concrete was considered as a uniform and isotropic continuous medium; thus the concrete skeleton was assumed as an impermeable material that did not react with gas or liquid phases. COMSOL®® software (COMSOL Inc., Stockholm, Sweden) was used to establish a three-dimensional numerical model based on Equations (25)–(28), and one-dimensional transmission was adopted. The physical parameters of heat and moisture transport are shown in Tables 6 and 7. The size of the simulated specimen was the same as that of the experimental specimen used in the test, namely 30 mm × 100 mm × 100 mm. A total of 9520 tetrahedral elements were used in COMSOL®® software to develop the finite element model with DOFs of 28,186 and convergence criteria of 10^{-5}, as shown in Figure 5.

Table 6. Heat transfer physical parameters.

Parameter	Dry Thermal Conductivity, λ_{a}(W/m·K)	Specific Heat, c (J/kg·K)	Concrete Density, ρ	Porosity, ϕ
Value	1.578	900	2297	0.1796

Table 7. Moisture transport physical parameters.

Parameter	Intrinsic Permeability, k (m^2)	Water Density, ρ_1 (kg/m^3)	Gas Constant R (J/mol·K)	Molar Mass of Water, M (kg/mol)
Value	1.413×10^{-21}	1000	8.3144	0.018

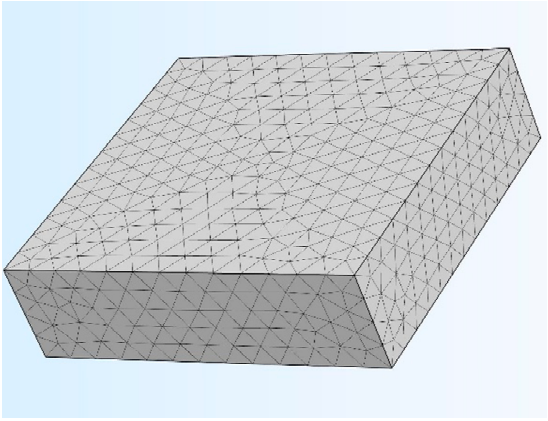

Figure 5. Mesh elements division of concrete.

5.2. Moisture Transport Model Validation

The experimental results shown in Figure 2 were simulated for 80% and 95% RH at 20, 35 and 50 °C to validate the moisture transport model. The initial internal saturation of the concrete was set as 0.08, and the boundary saturation was the corresponding equilibrium saturation. The initial temperature of inside concrete was 283.15 K, and the simulation time was the hygroscopic equilibrium time for the three temperatures, which was approximately 350 h. The simulated results were compared with the experimental results, as shown in Figure 6.

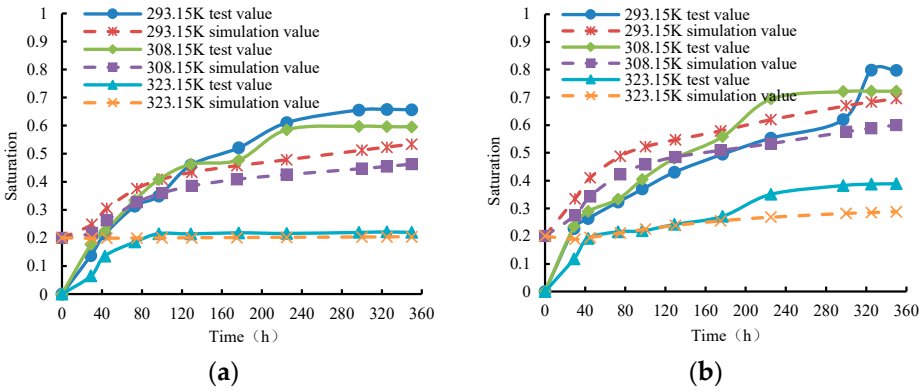

Figure 6. Test and simulation values of moisture absorption process: (**a**) is 80% RH, (**b**) is 95% RH.

The simulated and experimental results show a similar trend, and the values also agreed well. The simulated results were slightly lower than the experimental results. Under the simulated conditions, the moisture absorption rate decreased, and the moisture absorption capacity was slightly lower than that in the experiment. This could be because the moisture transport model only considers the transport of liquid water, not the moisture vapor transport that occurred under low-saturation conditions.

The experimental results provided in Figure 2 were applied to validate the moisture desorption model. The simulation was performed under the conditions of 10% and 35% RH at 20, 35 and 50 °C. The initial temperature inside the concrete was 283.15 K. The concrete interior was initially saturated and the boundary saturation was the corresponding equilibrium saturation. The simulation time was 250 h.

Figure 7 provides a comparison of the simulated and experimental results, which shows that the simulated values were in good agreement with the experimental values under 35% RH and were slightly higher than the experimental values at 10% RH. The overall results demonstrated that the simulated model of moisture desorption was valid. This also indicates that the simulated results remained accurate when the concrete was at a higher saturation level. When the saturation decreased, the simulated moisture desorption

rate was slightly lower than the experimental rate, implying that the water vapor transport in the concrete exerted limited influence under the low-saturation condition. In the marine environment, it is difficult for concrete to reach a low saturation state due to high RH. Therefore, the simulated model of moisture transport was accurate for the applications in the high RH environment.

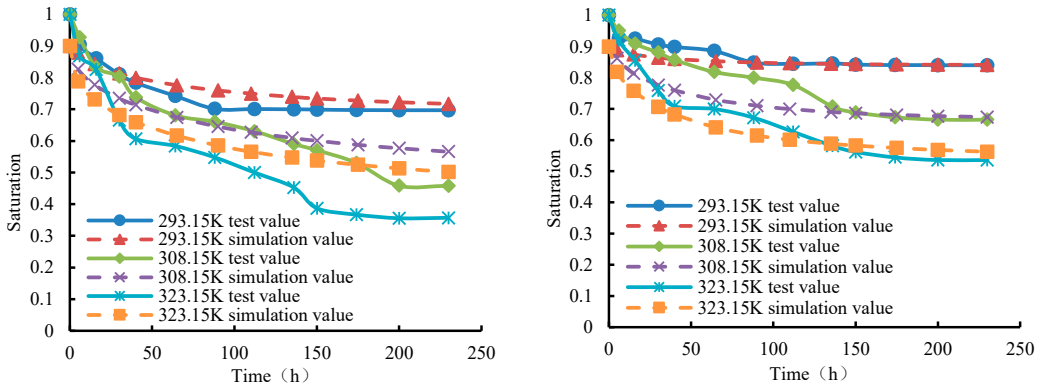

Figure 7. Test and simulation values of moisture desorption process: (**a**) is 10% RH, (**b**) is 35% RH.

5.3. Absorption

The upper, lower and right ends of the two-dimensional geometric model of concrete were defined as heat and moisture insulation. Therefore, moisture absorption was from left to inside. The effect of temperature on the moisture absorption process at 95% RH was evaluated under the temperatures of 293.15, 308.15 and 323.15 K and the boundary saturation values of 0.80, 0.72, and 0.39, respectively. The simulation had an initial temperature of 273.15 K, saturation of 0.2 and time of 500 days.

The simulated results are shown in Figure 8. It can be seen that the saturation was the lowest at 323.15 K (i.e., the highest temperature) but the highest at 293.15 K (i.e., the lowest temperature). For a given RH, an increased temperature decreased boundary saturation, moisture transport rate, moisture transport capacity, moisture transport distance and moisture absorption. The saturation gradient is the main driving potential of moisture transfer. A higher temperature reduced moisture absorption rate. Meanwhile, with temperature increasing, the equilibrium saturation of the concrete boundary further decreased. Such a combined effect decreased moisture absorption of concrete.

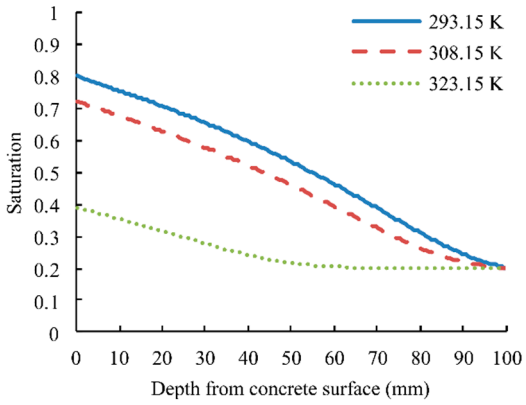

Figure 8. Simulated distribution at different temperatures.

The combined influences of the temperature and saturation in the moisture transport process were investigated at three conditions: high temperature and RH (boundary temperature T = 323.15 K, boundary saturation S = 0.9), medium temperature and RH (boundary

temperature T = 308.15 K, boundary saturation S = 0.75) and low temperature and RH (boundary temperature T = 293.15 K, boundary saturation S = 0.6). The simulation had an initial temperature of 273.15 K, saturation of 0.2 and time of 500 days. The simulated results are provided in Figure 9, which shows the same trend among the three conditions. The transport rate is directly correlated with temperature and RH. It also shows that the saturation gradient mostly affected moisture transport rate. Although the saturation was large at high temperature, the moisture transport rate was notably high. Therefore, the effect of RH on the moisture transport rate in the concrete was greater than that of temperature. The transport process of moisture in concrete at the temperature of 293.15 K and saturation 0.6 for simulation at 500d is shown in Figure 10. It can be seen that the moisture is gradually transferred from the left end of the concrete to the interior, and the saturation is reduced with depth increasing, which is coherent with the trend in Figure 9.

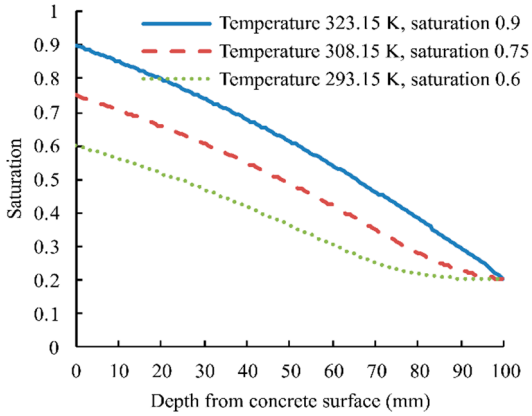

Figure 9. Saturation distribution during the absorption simulation.

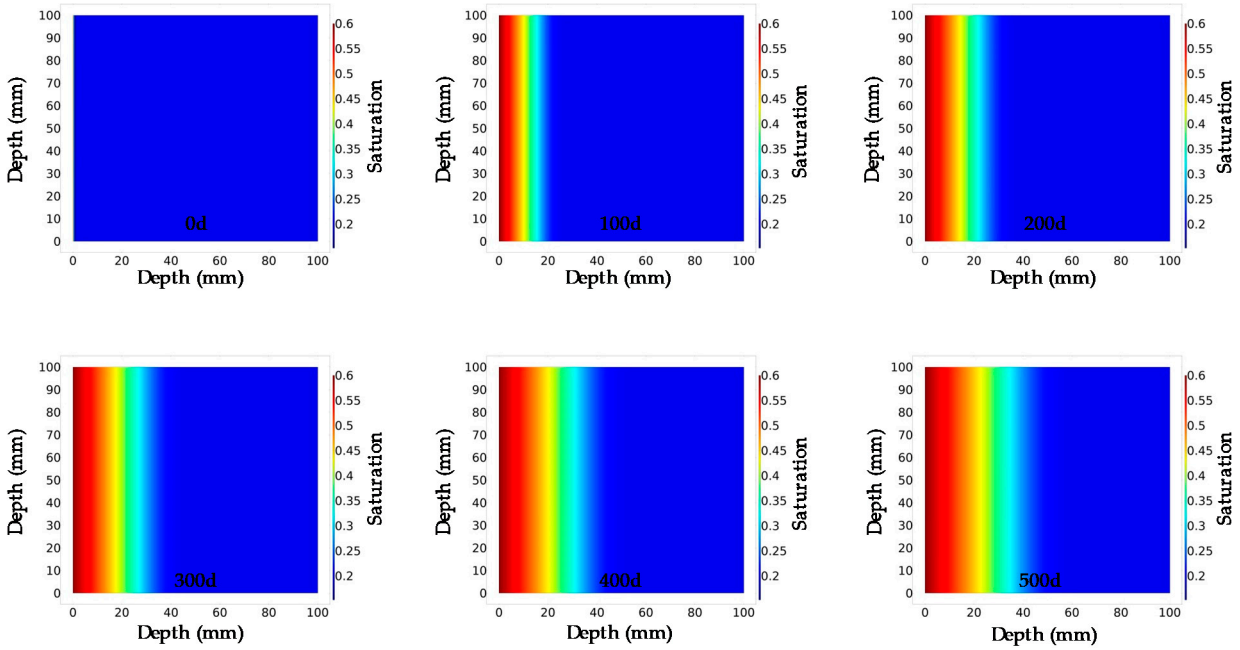

Figure 10. Cloud atlas of moisture in absorption process at temperature of 293.15 K and saturation of 0.6.

5.4. Desorption

The upper and lower ends of the two-dimensional geometric model of concrete were treated as heat and moisture insulation. The direction of moisture desorption was from inside to both sides. The effect of temperature on the moisture desorption process at 10%

RH was analyzed at temperatures of 293.15, 308.15 and 323.15 K and boundary saturation values of 0.70, 0.46 and 0.36, respectively. The simulation time was 200 days with an initial temperature of 273.15 K and saturation of 0.9.

Figure 11 presents the simulated results. It illustrates that, for a given RH, higher temperatures lowered the boundary saturation. When the internal saturation of concrete was higher, the difference in saturation was greater between the outside and inside of concrete, resulting in a significant loss of moisture in the concrete. The boundary saturation was lower at higher temperatures, which increased the moisture desorption rate as well as the moisture desorption capacity.

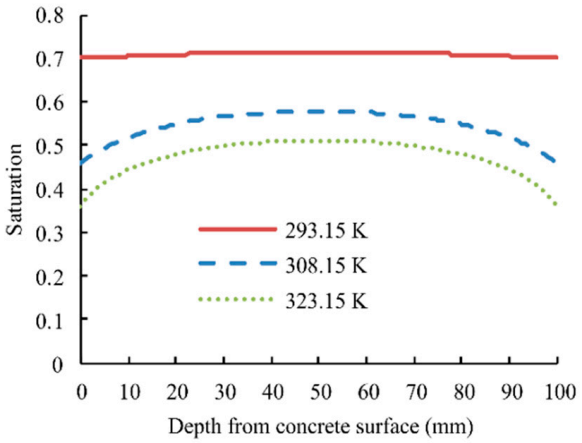

Figure 11. Saturation distribution during the desorption simulation.

Additionally, the combined effects of temperature and saturation on the moisture transport process during desorption were investigated for three conditions: low temperature and high RH (boundary temperature T = 293.15 K, internal saturation S = 0.9), medium temperature and RH (boundary temperature T = 308.15 K, internal saturation S = 0.75) and high temperature and low RH (boundary temperature T = 323.15 K, internal saturation S = 0.6). The simulation time was 500 days with an initial temperature of 273.15 K and saturation of 0.2.

As shown in Figure 12, the three curves displayed a similar trend. The saturation values for the three conditions at the internal depth of 50 mm were 0.552, 0.481 and 0.417, respectively. Even at low temperature, the greatest moisture transport rate was observed at the highest RH. The temperature had a greater effect on the moisture desorption process than saturation. The change of saturation of moisture in the desorption process at a temperature of 308.15 K and saturation of 0.75 is shown for the simulation at 500d in Figure 13. This indicates that the moisture was uniformly desorbed to both sides. The rate of saturation reduction was high close to both sides, while it was slow in the middle. This is due to the fact that the boundary temperature is higher at the concrete's surface, resulting in faster moisture transport.

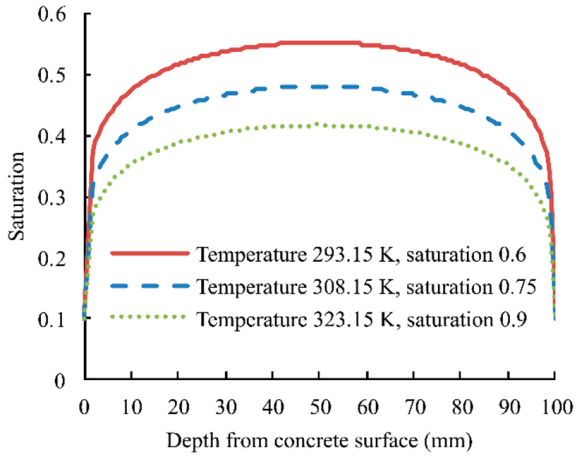

Figure 12. Internal average saturation distribution during the desorption process.

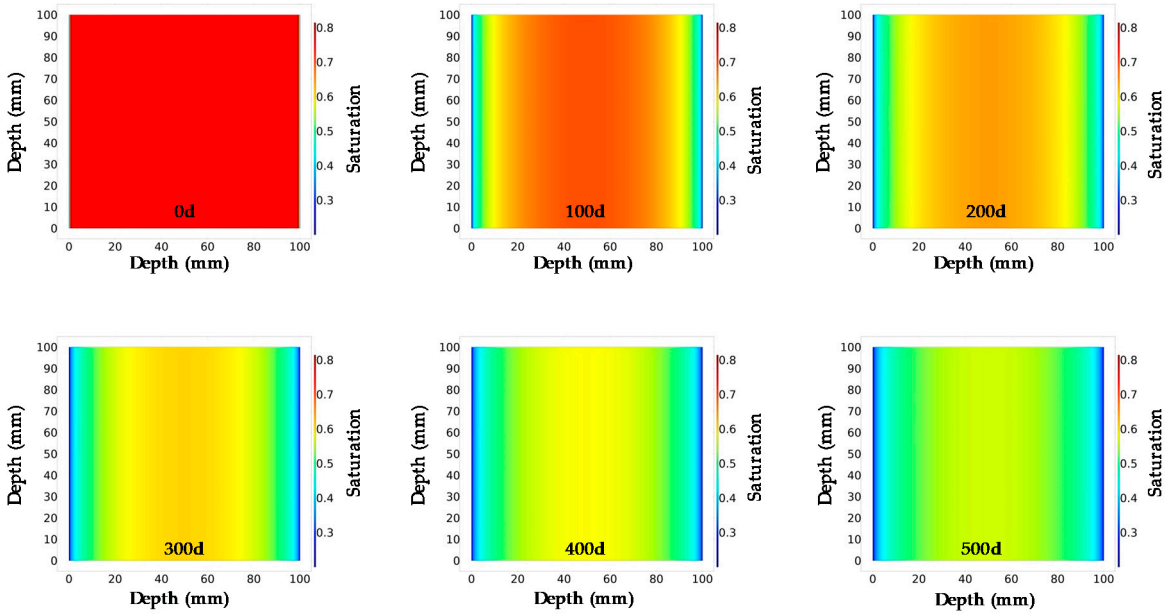

Figure 13. Cloud atlas of moisture in the desorption process at a temperature of 308.15 K and saturation of 0.75.

6. Conclusions

This study sought to elucidate the mechanisms of moisture transport in concrete. A numerical model was developed. Based on the experimental and simulated results, the following conclusions can be drawn.

(1) Under isothermal conditions, a higher RH increased the moisture absorption rate, and the moisture absorption capacity was greater at lower temperatures. When RH exceeded 50%, the moisture absorption rate increased significantly. Similarly, a lower RH resulted in a faster desorption, and higher temperatures increased the moisture desorption capacity.

(2) A model of the relationship between RH and equilibrium saturation in absorption and desorption processes was proposed. A formula in the function of capillary pressure and moisture saturation of concrete was established, and a model of moisture transport in the concrete was developed. The experimental results verified the accuracy of the moisture transport model.

(3) Based on the simulated results, an increased temperature reduced the rate of moisture absorption. The saturation had more effects on the absorption rate than tempera-

ture. Although an increment of temperature increased the moisture desorption rate, the saturation had more effects on the moisture desorption than temperature.

(4) Under low saturation, the transport of water vapor affected the moisture desorption rate in concrete. Hence, the transport of water vapor should be further considered in the moisture transport model.

Author Contributions: Conceptualization, Q.Z. and H.C.; investigation, Z.K.; data curation, Q.Z., Z.K. and K.L.; methodology, Q.Z.; visualization, Y.L.; formal analysis, Z.K.; software, K.L.; writing—original draft, Z.K.; writing—review and editing, Y.L., Q.Z., Z.K., H.C. and K.L.; project administration, Q.Z.; funding acquisition, Q.Z.; validation, Q.Z., Y.L. and H.C.; resources, H.C. All authors have read and agreed to the published version of the manuscript

Funding: This work was financially supported by the National Natural Science Foundation of China [grant number 51509084]; the Foundation of Key Laboratory of Performance Evolution and Control for Engineering Structures of Ministry of Education, Tongji University [grant number 2018KF-2]; the Cultivation Plan for Youth Backbone Teachers of Institution of Higher Education by Henan Province [grant number 2019GGJS086]; the Fundamental Research Funds for the Henan Provincial Colleges and Universities in Henan University of Technology [grant number 2017RCJH03]; the Cultivation Plan for Youth Backbone Teachers by Henan University of Technology; and the Innovative Funds Plan of Henan University of Technology (Grant No. 2020ZKCJ05).

Conflicts of Interest: The authors declare no conflict of interest.

References

1. Kodur, V.; Naser, M. *Structural Fire Engineering*; MGH Press: New York, NY, USA, 2020. Available online: https://www.researchgate.net/publication/340183424_Structural_Fire_Engineering (accessed on 22 December 2020).
2. Khoury, G. Passive fire protection in tunnels. *Concrete* **2003**, *37*, 31–36.
3. Kodur, V.; Phan, L. Critical factors governing the fire performance of high strength concrete systems. *Fire Saf. J.* **2007**, *42*, 482–488. [CrossRef]
4. Zhang, Y.; Ye, G. A model for predicting the relative chloride diffusion coefficient in unsaturated cementitious materials. *Cem. Concr. Res.* **2019**, *115*, 133–144. [CrossRef]
5. Homan, L.; Ababneh, A.N.; Xi, Y. The effect of moisture transport on chloride penetration in concrete. *Constr. Build. Mater.* **2016**, *125*, 1189–1195. [CrossRef]
6. Li, K.; Li, C.; Chen, Z. Influential depth of moisture transport in concrete subject to drying–wetting cycles. *Cem. Concr. Compos.* **2009**, *31*, 693–698. [CrossRef]
7. Baroghel-Bouny, V. Water vapour sorption experiments on hardened cementitious materials: Part I: Essential tool for analysis of hygral behaviour and its relation to pore structure. *Cem. Concr. Res.* **2007**, *37*, 414–437. [CrossRef]
8. Zeng, Q.; Wang, Y.; Li, K. Uniform model for moisture transport in porous materials and its application to concrete at selected Chinese regions. *J. Mater. Civ. Eng.* **2014**, *26*, 05014001. [CrossRef]
9. Li, C. Study on Water and Ionic Transport Processes in Cover Concrete under Drying-Wetting Cycles. Ph.D. Thesis, Tsinghua University, Beijing, China, 2009.
10. Ishida, T.; Maekawa, K.; Kishi, T. Enhanced modeling of moisture equilibrium and transport in cementitious materials under arbitrary temperature and relative humidity history. *Cem. Concr. Res.* **2007**, *37*, 565–578. [CrossRef]
11. Černý, R.; Rovnanikova, P. *Transport Processes in Concrete*, 1st ed.; CRC Press: London, UK, 2002. [CrossRef]
12. Trabelsi, A.; Belarbi, R.; Turcry, P.; Aït-Mokhtar, A. Water vapour desorption variability of in situ concrete and effects on drying simulations. *Mag. Concr. Res.* **2011**, *63*, 333–342. [CrossRef]
13. Neithalath, N.; Sumanasooriya, M.S.; Deo, O. Characteriz ing pore volume, sizes, and connectivity in pervious concretes for permeability prediction. *Mater. Charact.* **2010**, *61*, 802–813. [CrossRef]
14. Baroghel-Bouny, V.; Mainguy, M.; Lassabatere, T.; Coussy, O. Characterization and identification of equilibrium and transfer moisture properties for ordinary and high-performance cementitious materials. *Cem. Concr. Res.* **1999**, *29*, 1225–1238. [CrossRef]
15. Van Genuchten, M.T. A closed-form equation for predicting the hydraulic conductivity of unsaturated soils. *Soil Sci. Soc. Am. J.* **1980**, *44*, 892–898. [CrossRef]
16. Zhou, C.; Li, K. Numerical and statistical analysis of permeability of concrete as a random heterogeneous composite. *Comput. Concr.* **2010**, *7*, 469–482. [CrossRef]
17. Wang, L.; Ueda, T. Mesoscale modeling of water penetration into concrete by capillary absorption. *Ocean Eng.* **2011**, *38*, 519–528. [CrossRef]
18. Li, X.; Xu, Y.; Chen, S. Computational homogenization of effective permeability in three-phase mesoscale concrete. *Constr. Build. Mater.* **2016**, *121*, 100–111. [CrossRef]

19. Zhang, Q.; Tian, S.; Li, K.; Li, Z. Experiment and analysis of thermal conductivity of marine concrete with different composition. *IOP Conf. Ser. Earth Environ. Sci.* **2019**, *242*, 1–6. [CrossRef]
20. Wu, Q.; Yu, H. Rebar corrosion rate estimation of reinforced concrete components exposed to marine environment. *Strength Mater.* **2019**, *51*, 653–659. [CrossRef]
21. Cheewaket, T.; Jaturapitakkul, C.; Chalee, W. Initial corrosion presented by chloride threshold penetration of concrete up to 10 year-results under marine site. *Constr. Build. Mater.* **2012**, *37*, 693–698. [CrossRef]
22. BSI Standards Publication. ISO 12571:2013 Hygrothermal Performance of Building Materials and Products—Determination of Hygroscopic Sorption Properties, CEN-CENELEC Management Centre. 2013. Available online: https://www.iso.org/cms/render/live/en/sites/isoorg/contents/data/standard/06/13/61388.html (accessed on 22 December 2020).
23. Wei, X.; Jin, L.; Zhang, Y.; Ding, Z. Water transport in cracked unsaturated concrete. *J. Build. Mater.* **2018**, *21*, 725–731. [CrossRef]
24. Schiller, P.; Wahab, M.; Bier, T.; Mögel, H.-J. A model for sorption hysteresis in hardened cement paste. *Cem. Concr. Res.* **2019**, *123*, 105760. [CrossRef]
25. Jiang, Z.; Xi, Y.; Gu, X.; Huang, Q.; Zhang, W. Modelling of water vapour sorption hysteresis of cement-based materials based on pore size distribution. *Cem. Concr. Res.* **2019**, *115*, 8–19. [CrossRef]
26. Ranaivomanana, H.; Verdier, J.; Sellier, A.; Bourbon, X. Toward a better comprehension and modeling of hysteresis cycles in the water sorption–desorption process for cement based materials. *Cem. Concr. Res.* **2011**, *41*, 817–827. [CrossRef]
27. Poyet, S. Experimental investigation of the effect of temperature on the first desorption isotherm of concrete. *Cem. Concr. Res.* **2009**, *39*, 1052–1059. [CrossRef]
28. Yu, C. *Numerical Analysis of Heat and Mass Transfer for Porous Materials*, 1st ed.; THU Press: Beijing China, 2011.
29. Baroghel-Bouny, V. Water vapour sorption experiments on hardened cementitious materials. Part II: Essential tool for assessment of transport properties and for durability prediction. *Cem. Concr. Res.* **2007**, *37*, 438–454. [CrossRef]
30. Daian, J.-F. Condensation and isothermal water transfer in cement mortar Part I—Pore size distribution, equilibrium water condensation and imbibition. *Transp. Porous Media* **1988**, *3*, 563–589. [CrossRef]
31. Ji, Z.; Zhu, R.; Li, D. *Transmission Principle*, 1st ed.; HIT Press: Harbin, China, 2017.
32. Savage, B.M.; Janssen, D.J. Soil physics principles validated for use in predicting unsaturated moisture movement in Portland cement concrete. *Mater. J.* **1997**, *94*, 63–70. [CrossRef]
33. Jerman, M.; Černý, R. Effect of moisture content on heat and moisture transport and storage properties of thermal insulation materials. *Energy Build.* **2012**, *53*, 39–46. [CrossRef]